Available online at www.sciencedirect.com
SCIENCE DIRECT®
Journal of Nuclear Materials 351 (2006) 197–208
journal of nuclear materials
www.elsevier.com/locate/jnucmat

Positron annihilation spectroscopy and small angle neutron scattering characterization of nanostructural features in high-nickel model reactor pressure vessel steels

Stephen C. Glade [a], Brian D. Wirth [a,*], G. Robert Odette [b], P. Asoka-Kumar [c]

[a] *Nuclear Engineering Department, University of California, Berkeley, CA 94720-1730, USA*
[b] *University of California, Santa Barbara, CA, USA*
[c] *Lawrence Livermore National Laboratory, Livermore, CA, USA*

Abstract

Irradiation embrittlement in nuclear reactor pressure vessel steels results from the hardening by a high number density of nanometer scale features. In steels with more than ≈0.10% Cu, the dominant features are often Cu-rich precipitates typically alloyed with Mn, Ni and Si. At low-Cu and low-to-intermediate Ni levels, so-called matrix hardening features are believed to be vacancy-solute cluster complexes, or their remnants. However, Mn–Ni–Si rich precipitates, with Mn plus Ni contents greater than Cu, can form at high alloy Ni contents and are promoted at irradiation temperatures lower than the nominal 290 °C. Even at very low-Cu levels, late blooming Mn–Ni–Si rich precipitates are a significant concern due to their potential to form large volume fractions of hardening features. Positron annihilation spectroscopy (PAS) and small angle neutron scattering neutron (SANS) measurements were used to characterize the fine-scale microstructure in split-melt A533B steels with varying Ni and Cu contents, irradiated at selected conditions from 270 to 310 °C between ≈0.04 and 1.6×10^{23} n m^{-2}. The objective was to assess the character, composition and magnetic properties of Cu-rich precipitates, as well as to gain insight on the matrix features. The results suggest that the irradiated very low-Cu and intermediate Ni steel contains small vacancy-Mn–Ni–Si cluster complexes, but not large, well-formed and highly enriched Mn–Ni–Si phases. The hardening features in steels containing 0.2% and 0.4% Cu, and 0.8% and 1.6% Ni are consistent with well-formed, non-magnetic Cu–Ni–Mn precipitates. The precipitate number densities and volume fractions increase, while their sizes decrease, with increasing Ni and decreasing irradiation temperature. The precipitates evolve with fluence in stages of nucleation, growth and limited coarsening.

1. Introduction

Western reactor pressure vessel (RPV) steels are fabricated from quenched and tempered C–Mn–Si–Mo–Ni low-alloy bainitic steels. RPVs operate at around 290 °C accumulating fast neutron fluences from about 1 to 10×10^{23} n m^{-2} over a 40–60 year service life, corresponding to a maximum damage dose less than ≈0.15 displacements per atom (dpa) [1–4]. However, even this relatively low dose is sufficient to produce severe embrittlement in some cases, characterized by upward shifts

* Corresponding author. Tel.: +1 510 642 5341; fax: +1 510 643 9685.
E-mail address: bdwirth@nuc.berkeley.edu (B.D. Wirth).

0022-3115/$ - see front matter © 2006 Elsevier B.V. All rights reserved.
doi:10.1016/j.jnucmat.2006.02.012

in the transition temperature (ΔT) between the more brittle cleavage and more ductile microvoid coalescence fracture regimes.

Embrittlement is primarily the result of irradiation hardening, reflected in yield strength increases, with corresponding ΔT values of 300 °C or more. Embrittlement is controlled by a complex combination of variables, including the neutron flux, fluence and energy spectrum, the irradiation temperature (irradiation variables), and the alloy's starting microstructure and composition (material variables) [1–6]. Important compositional variables include Cu (0.02–0.5%), Ni (0.2–2%) and Mn (0.3–2%), while P (0.005–0.040%) and Si (0.2–0.7%) generally play secondary roles (note all compositions in this paper are given in weight percent unless otherwise noted). The principal source of irradiation hardening is the formation of high number densities of nanometer-sized irradiation-induced precipitates and so-called matrix features, which impede the motion of dislocations [1–6]. In Cu-bearing steels, irradiation hardening is primarily associated with the accelerated formation of nanometer-sized Cu-rich precipitates (CRPs) due to radiation-enhanced solute diffusion. The CRPs are enriched in Ni, Mn and Si. Mn–Ni rich precipitates (MNPs) containing a range of Cu, as dictated by the alloy content of this element, form at high alloy Mn and Ni levels, and are promoted by lower irradiation temperatures (<290 °C) and Cu contents [2,7]. Indeed, nearly pure well-formed Mn–Ni–Si phases develop even in very low-Cu steels at sufficiently high fluence and Ni contents (possibly > 1%), although the temperature–alloy composition MNP phase boundaries have not been experimentally established. Smaller, so-called matrix features, believed to be vacancy-solute (e.g., Mn, Ni and Si) cluster complexes, or their solute remnants, also contribute to hardening, even in alloys with low or no copper [3,8]. The matrix features may be precursors to MNP formation.

The CRPs [9] and MNPs [1], first predicted by Odette, have been identified and characterized by a combination of experimental techniques, including small angle neutron scattering (SANS) [2,10–13], atom probe field ion microscopy (APFIM) [13–19], combined electrical resistance Seebeck coefficient measurements (RSC) [19–21], and recently, positron annihilation spectroscopy (PAS) [22–26]. The characteristics of the CRPs and MNPs have been studied as a function of steel composition, heat treatment, irradiation temperature, neutron flux and fluence. In general, the results derived from the different techniques are in good agreement, although some questions remain regarding the composition of the precipitates, particularly with respect to their possible Fe content [13]. Specifically, some atom probe data has been interpreted to suggest the precipitates contain up to 50% or more Fe, which is inconsistent with the results of other techniques. It is believed that some Cu catalyzes MNP formation, but they can also form even in steels with little or no Cu at sufficiently high fluence, depending on the irradiation temperature and alloy Ni and Mn content. Once nucleated, MNPs grow rapidly to large volume fractions, with a correspondingly high level of hardening and embrittlement [1,2]. However, a complete understanding of the necessary conditions for MNP formation and evolution as a function of irradiation and material variables does not yet exist.

In this paper, we present the results of a positron annihilation spectroscopy (PAS) and small angle neutron scattering (SANS) study to characterize the nanometer precipitates and matrix features formed in a series of model RPV steels with controlled variations in Cu and Ni contents following selected neutron irradiation at a flux of $3.2 \pm 0.6 \times 10^{15}$ n m^{-2} s^{-1} to fluences from 0.04 to 1.6×10^{23} n m^{-2} over the temperature range of 270–310 °C. The results, which extend our previous measurements on model alloys, provide quantitative information on the composition, sizes, number densities, volume fractions and magnetic properties of the Cu–Ni–Mn precipitates (CRPs), as well as further qualitative insight on the matrix features.

2. Experimental methods

2.1. Materials and irradiations

Commercial model (CM) A533B-type split-melt bainitic steels with controlled variations in Cu and Ni content, as shown in Table 1, were examined in this study. The matrix consisted of a low-Cu, intermediate Ni steel (CM3) and intermediate (CM16 and CM17) and high (CM19 and CM20) Cu alloys with both intermediate (CM16 and CM19) and high (CM17 and CM20) Ni contents. These CM-series steels had typical prior austenite grain sizes of ≈50 μm and tempered bainite microstructures. The heat treatment schedule was as follows: austenitize at 900 °C for 0.5 h, salt bath quench to 450 °C and hold for 600 s, temper at 660 °C for 4 h, stress

Table 1
Measured compositions of the model steels used in this study

Steel	Cu (wt%)	Ni (wt%)	Mn (wt%)	Mo (wt%)	C (wt%)	P (wt%)	Si (wt%)	S (wt%)
CM3	0.02 (low)	0.85 (intermediate)	1.60	0.49	0.13	0.006	0.16	0.000
CM16	0.22 (intermediate)	0.82 (intermediate)	1.58	0.51	0.16	0.004	0.25	0.000
CM17	0.22 (intermediate)	1.59 (high)	1.54	0.50	0.16	0.004	0.25	0.000
CM19	0.42 (high)	0.85 (intermediate)	1.63	0.51	0.16	0.005	0.16	0.003
CM20	0.43 (high)	1.69 (high)	1.63	0.50	0.16	0.006	0.16	0.003

All values are given in weight percent.

relieve at 607 °C for 24 h, cool at 8 °C/h to 300 °C. Air cooling followed all the steps in the heat treatment sequence described above.

Approximately $1 \times 1 \times 0.2$ cm coupons were neutron irradiated in the University of California, Santa Barbara (UCSB) irradiation variable (IVAR) experiment at the University of Michigan Ford Nuclear Reactor. The neutron fluxes, fluences and irradiation temperatures are shown in Table 2. The irradiations provided a systematic variation in fluence from 4.0×10^{21} to 1.6×10^{23} n m^{-2} (T11, T12, T14, and T16) at a nominal flux of 3×10^{15} n m^{-2} s^{-1} and 290 °C, as well as a systematic variation in irradiation temperature from 270 to 310 °C (T16, T18, and T20) at the same flux and a fluence of 1.6×10^{23} n m^{-2}.

2.2. Positron annihilation spectroscopy (PAS)

PAS is a well-established technique for detecting open-volume regions in a material [27], as well as the chemical identity of the elements at the annihilation site [28]. After they thermalize, positrons either annihilate in the matrix or localize in open-volume regions (vacancies, nanovoid clusters, and other defects with regions of dilatational strain) due to the 'absence' of positively charged atomic nuclei. Such trapped positrons also have a longer lifetime due to the lower electron density in the open-volume defects. Since each element has a unique positron affinity, second phase precipitates may have higher (or lower) positron affinity than the matrix they are embedded in, also leading to positron localization in these regions. In this study of model A533B-type steels, the positron affinities of the key elements are: −3.72 eV Mn, −3.84 eV Fe, −4.46 eV Ni and −4.81 eV Cu [29]. As shown by Nagai et al. [22], PAS is an especially well suited technique for studying CRPs, since Cu clusters as small as ~0.6 nm embedded in an Fe matrix effectively localize and strongly trap positrons.

Table 2
Neutron irradiation conditions used in this study

	Neutron flux [ϕ (n m^{-2} s^{-1})]	Neutron fluence [ϕ (n m^{-2})]	T (°C)
T11	2.6×10^{15}	4.0×10^{21}	290
T12	3.2×10^{15}	1.0×10^{22}	290
T14	3.2×10^{15}	4.8×10^{22}	290
T16	3.0×10^{15}	1.6×10^{23}	290
T18	3.6×10^{15}	1.7×10^{23}	270
T20	3.4×10^{15}	1.6×10^{23}	310

Ultimately, the positron annihilates with an electron, predominately yielding two ~511 keV photons traveling in approximately opposite directions. The photons carry information about the positron annihilation site. The momentum of the electron (primarily)-positron (thermalized) pair prior to annihilation produces a Doppler shift (blue-shift and a red-shift) of the two annihilation photons. The energy shift of each photon is given by

$$\Delta E = \frac{1}{2} p_L c = \frac{1}{2} \theta_L m_0 c^2. \quad (1)$$

Here ΔE is the photon energy difference from the nominal value, p_L is the corresponding longitudinal momentum shift along the direction of the gamma ray emission, θ_L is the angular deviation of the photons from 180°, m_0 is the electron rest mass, and c is the speed of light. The p_L is expressed here in atomic units (1 a.u. = 7.28 mrad × $m_0 c$). The coincidence Doppler broadening (CDB) technique is used to evaluate ΔE, hence p_L, by simultaneously measuring the two photon energies. Since the p_L have element specific spectral distributions that correspond to the momentum distributions of the annihilation electrons, analysis of the orbital electron momentum spectrum (OEMS) provides information on the local composition at the annihilation site, including those in strong positron traps. The OEMS is typically represented as the fraction of annihilations (relative number of counts) at each momentum interval as a function of p_L, $n(p_L)$, normalized by a standard spectrum, in our case that for nominally

pure and defect free Fe, $n_{Fe}(p_L)$, or $n(p_L)/n_{Fe}(p_L)$. In transition metals in the Fe-series, lattice annihilations preferentially occur with 3d orbital electrons. The maxima and minima of the $n(p_L)/n_{Fe}(p_L)$ OEMS are specific to a given element. For example, the normalized OEMS of Cu and Ni have peaks at an intermediate position in the high-momentum region. In contrast, other elements, such as Mn, have a minimum in the Fe-normalized OEMS at high momentum. Since annihilations in vacancies and vacancy cluster traps occur primarily with the delocalized valence electrons of the surrounding atoms, the corresponding OEMS are characterized by the enhancement of the low-momentum region.

Mixtures of elements and vacancies have OEMS that are approximately the constituent fraction based averages, weighted by factors that reflect their relative affinities. The weighting can be determined from first principles quantum mechanical calculations. Measured OEMS also reflect a competition between various annihilation sites, including the matrix and various higher affinity traps. Positrons generally do not detect low affinity features. Finally, positrons may either localize within a sub-region of a compositionally non-uniform precipitate or defect-solute complex, or the positron wave function may be incompletely confined (leak out into the surrounding matrix) of very small trapping features. For example, positrons would tend to be localized in nearly pure Cu-rich core of a CRP, hence not fully detect enrichment of Mn, Ni and Si atoms in a surrounding shell. In both cases, the overall OEMS is a spatially and affinity weighted combination of the constituents comprising the feature.

In addition to $n(p_L)/n_{Fe}(p_L)$ versus p_L plots, it is convenient to represent OEMS data in so-called S–W plots. The S is a fraction of low-momentum annihilations defined by specified p_L limits, which in our case is $p_L \leqslant 0.382$ a.u., and W is the corresponding high-momentum annihilation fraction as specified by a corresponding second set of p_L limits, here $1.0 \leqslant p_L \leqslant 4.0$ a.u. A particular microstructure produces a point on a S–W plot. The weighting of two elements (or annihilation sites, including defects) is shown by the position of the specimen point on a line joining the pure elements (and/or sites).

The CDB measurements were performed at Lawrence Livermore National Laboratory (LLNL) using an experimental setup in which positrons emitted from a ^{22}Na radioactive source are confined and transported to the specimen using a strong magnetic field (~1.0 kG). The magnetic field can also be used to perform so-called spin-polarized, magnetic positron annihilation measurements [24], yielding data on the magnetic character at the positron annihilation site. The magnetic field is alternately oriented parallel and anti-parallel to the positron spin. Changes in the majority and minority electron populations in a ferromagnetic material with magnetic field reversal, combined with the fact that electron–positron annihilation only produces two annihilation photons when the respective spins are anti-parallel, results in corresponding differences in the OEMS measured by CDB. When the OEMS data are represented in S–W plots, the two data points, associated with each magnetic field orientation, are split. Non-magnetic annihilation sites have almost identical OEMS and S–W plot positions for the parallel and anti-parallel magnetic field orientations, while annihilations at atoms with different majority–minority electron spins show a characteristic S–W splitting. The observed degree of splitting is again a function of the weighting of the various constituents in an annihilation site and between various trapping sites.

2.3. Small-angle neutron scattering (SANS)

SANS was performed at the 8-m (NG1) beamline at the Cold Neutron Research Facility of the National Institute of Standards and Technology [30]. The un-irradiated (control) materials and the irradiated samples were each measured in a strong magnetic field ($\geqslant 1.8$ T) oriented horizontally to saturate the α-Fe matrix. This allows for measurement of both the nuclear (N) and magnetic (M) neutron cross-sections as a function of the scattering vector, q, which results from the corresponding nuclear and magnetic scattering length density differences between the α-Fe matrix and the feature. The neutron scattering at small angles ($\theta \leqslant 8°$) was measured from a well-collimated beam of cold neutrons ($\lambda \approx 0.5$ nm) with a two-dimensional 64×64 cm position sensitive detector positioned ~2 m from the sample, and rotated 5° off-axis to increase the measured q-range.

After correcting the measured SANS data for background and parasitic scattering, the small angle scattering produced by the irradiation-induced features was isolated by subtracting the corresponding scattering signal of the appropriate unirradiated (control) specimen from that of the irradiated spec-

imen. The resulting irradiation-induced feature scattering was converted to an absolute scattering cross-section using the measured scattering from an isotropic scattering water specimen with a known cross-section ($= 0.88\ \mathrm{cm}^{-1}\ \mathrm{ster}^{-1}$).

The nanometer Cu–Ni–Mn precipitates are assumed to be roughly spherical and non-magnetic in a saturated ferromagnetic iron matrix, providing a known magnetic scattering contrast. A log-normal size distribution is fit to the absolute scattering cross-section data as a function of q. The slope curvature of the scattering curves determines the mean size ($\langle r \rangle$) and size distribution of the features, while the absolute scattering intensity determines the corresponding number density (N_d) and volume fraction (f_v). Further, the measured magnetic to nuclear scattering ratio (M/N) provides information on the scattering feature composition. Additional details regarding the SANS experiments and data analysis can be found elsewhere [13,31–33].

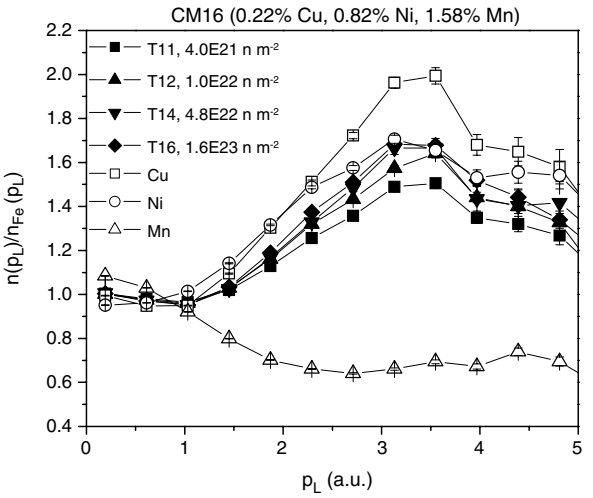

Fig. 1. Normalized OEMS of the intermediate-Cu, intermediate-Ni steel (CM16) under irradiations with increasing fluence from 4.0×10^{21} to $1.6 \times 10^{23}\ \mathrm{n\ m}^{-2}$ (T11, T12, T14, and T16). The correspondingly normalized curves for elemental Cu, Ni, and Mn are shown for comparison.

3. Results

3.1. PAS results

Fig. 1 presents the $n(p_L)/n_{Fe}(p_L)$ OEMS obtained as a function of increasing fluence from 4.0×10^{21} to $1.6 \times 10^{23}\ \mathrm{n\ m}^{-2}$ for the model steel containing intermediate concentrations of Cu and Ni (CM16 with 0.22% Cu, 0.82% Ni) irradiated at 290 °C. The normalized OEMS for the Fe reference specimen would correspond to a horizontal line at 1.0. Fig. 1 also shows the corresponding normalized OEMS of well-annealed elemental Cu, Ni, and Mn. The normalized OEMS for the irradiated steels show a broad peak at $p_L \approx 3.25$ a.u., consistent with positron localization in features containing Cu and Ni. The magnitude of the peak at $p_L \approx 3.25$ a.u. increases with increasing fluence up to a value about 90% of the average Cu–Ni peak height at a fluence of $4.8 \times 10^{22}\ \mathrm{n\ m}^{-2}$, and then remains approximately constant at higher fluence. It is well known that there is Mn (and Si) in the precipitates [1–3,13,15,34]. Thus the results can be interpreted as follows. The OEMS peak initially increases with fluence due to the increase in the size and number density of precipitate trapping sites and corresponding decrease in the competing annihilations in the Fe matrix. At higher fluence, the peak OEMS values are roughly consistent with 70% of the annihilations with Cu and 15% with each Ni and Mn. These values are reasonably close to estimates of the CRP composition from SANS M/N ratios [13] and resistivity Seebeck coefficient measurements [19], as well as thermodynamic calculations [1,4]. However, due to the elemental affinity differences, the annihilations do not scale in direct proportion to the atomic fractions. No increase in the low-momentum OEMS region, indicative of positron trapping and annihilation in vacancies and vacancy clusters, is observed. The OEMS trends shown in Fig. 1 are broadly consistent with those observed in other Fe–Cu–Ni–Mn model alloys and steels [25,31,35], including the intermediate-Cu, high-Ni steel (CM17, 0.22% Cu, 1.59% Ni) measured in this study, but not shown.

Fig. 2 presents the normalized OEMS for all the CM steels as a function of increasing irradiation temperature from 270 to 310 °C at $\approx 1.6 \times 10^{23}\ \mathrm{n\ m}^{-2}$. In all cases, the high-momentum OEMS peak increases significantly between 270 and 290 °C and slightly between 290 and 310 °C. The OEMS peak also shows slight, but systematic, increases with higher Cu and decreases with higher Ni. Both the temperature and composition trends are consistent with expected changes in the precipitate composition: higher temperature and Cu results in smaller quantities of Mn and Ni in the CRPs, while higher Ni decreases the Cu content of the precipitates, resulting in MNPs versus CRPs. Note the similarities between the alloys with intermediate and high bulk Cu levels are partly due to the fact that the actual Cu in solution prior to irradiation only varies

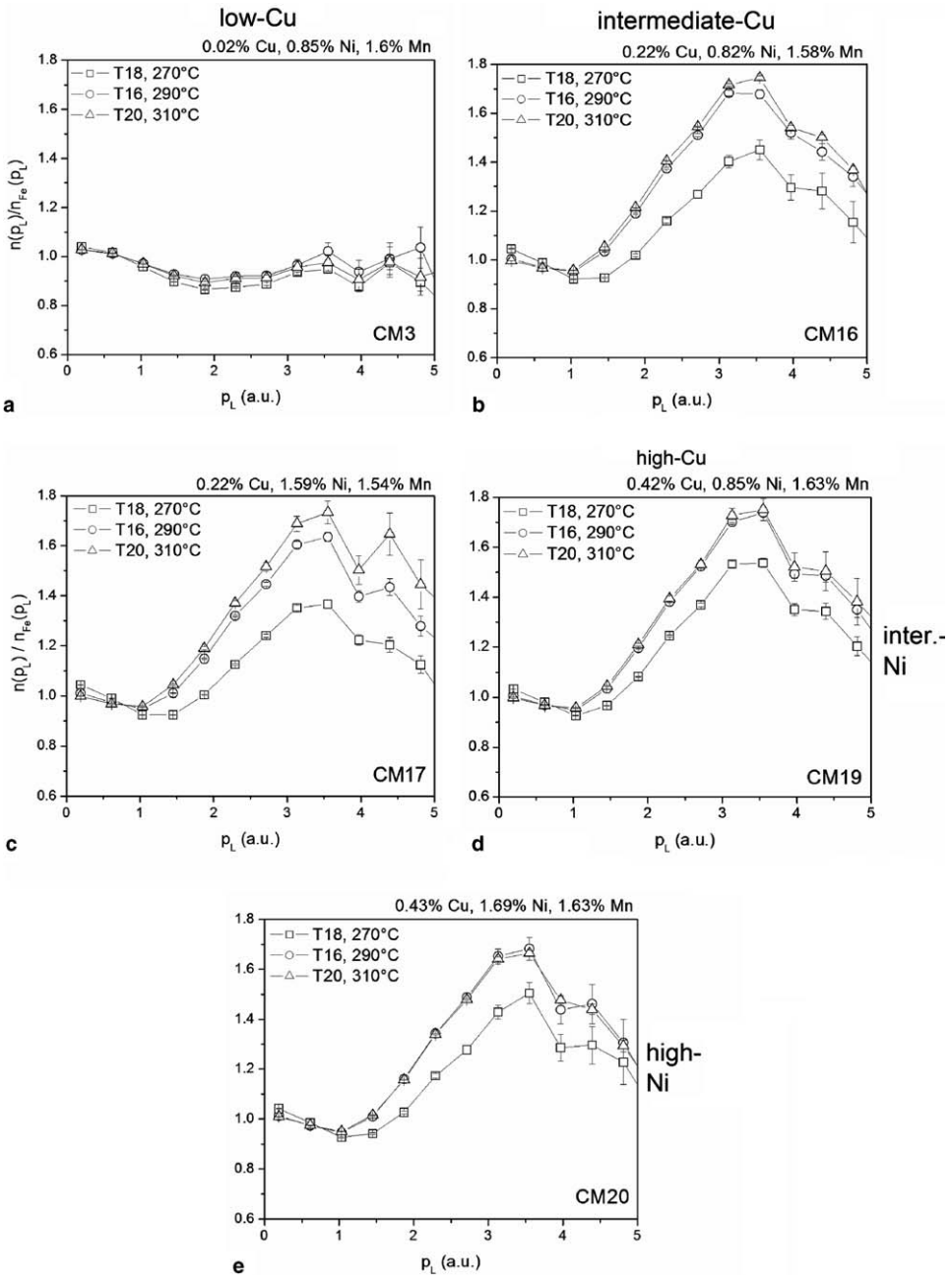

Fig. 2. Normalized OEMS of all steels in this study [(a) CM3, (b) CM16, (c) CM17, (d) CM19, and (e) CM20] under irradiation conditions with variations in temperature (270 °C – T18, 290 °C – T16, and 310 °C – T20). The nominal neutron fluence of these irradiations was 1.6×10^{23} n m^{-2}.

from ≈0.22% versus 0.25% to 0.31%, respectively. Similar, but somewhat larger differences in the OEMS peak would be expected based on the actual precipitate composition trends with changes in temperature and alloy solute content, assuming the annihilations scale directly with the atomic fractions in the trapping feature. However, the (oversimplified) assumption of preferential annihilations with Cu and Ni versus Mn qualitatively rationalize the somewhat lower compositional and temperature sensitivity of the OEMS peak. The other notable feature in the OEMS for the Cu-bearing alloys is

that there is a slight enhancement of the low-momentum region for the 270 °C irradiation. As discussed below this could be due to enhanced annihilations with vacancies, Mn or some combination of both. This observation is consistent with the expectation that the fractions of both of these constituents are expected to increase in the irradiation-induced features at lower temperature.

In contrast to the behavior of the Cu-bearing alloys, the normalized OEMS of the very low-Cu steel (CM3 with 0.02% Cu and 0.85% Ni) has a shallow minimum at higher momentum and a small enhancement at low momentum. This OEMS behavior is consistent with positron annihilation in some combination of vacancies, small vacancy clusters, and vacancy-solute clusters containing Ni, Si and Mn. While the positron affinity is low for Mn, it seems likely that positrons that do not annihilate in the matrix or at defects, such as dislocations and interfaces, would be trapped by very small vacancy cluster-solute complexes. Note, that positron interaction and annihilation with Si atoms will be analogous to that with a vacancy due to a combination of high affinity (−6.95 eV) [27] and an OEMS curve similar to Mn. Indeed at high momentum the $n(p_L)/n(p_L)_{Fe}$ (<0.5) for Si is lower than that for Mn while Si has a slightly larger (≈0.25) peak at low momentum [36]. Thus, in the case of the low-Cu CM3 alloys, the OEMS likely reflects some weighting of a mixture of vacancies, Ni, Mn, Si and Fe as well as a balance between annihilations in the matrix and small trapping features.

The results of spin-polarized, magnetic positron annihilation measurements are presented in the *S*–*W* plots in Fig. 3. Ferromagnetic Fe and Ni both exhibit splitting between the measurements with the magnetic field oriented parallel (up-triangle) and anti-parallel (down-triangle) relative to the positron spin, while the points for non-magnetic Cu and Mn fully overlap. As expected, the un-irradiated steels exhibit a split similar to that of elemental Fe. The splitting in irradiated low-Cu, intermediate-Ni steel (CM3) shown in Fig. 3(a) is similar to that in the unirradiated alloy. However, the data falls on the line roughly connecting Ni and Mn, and passing close to points for the unirradiated steel. The position of the data points between the unirradiated steel and Mn suggests enhanced annihilations at the latter. Note the point for vacancy features is not shown, but lies close to Mn on the *S*–*W* plot. The corresponding point for Si falls off the plot in the direction of a smaller high-momentum fraction

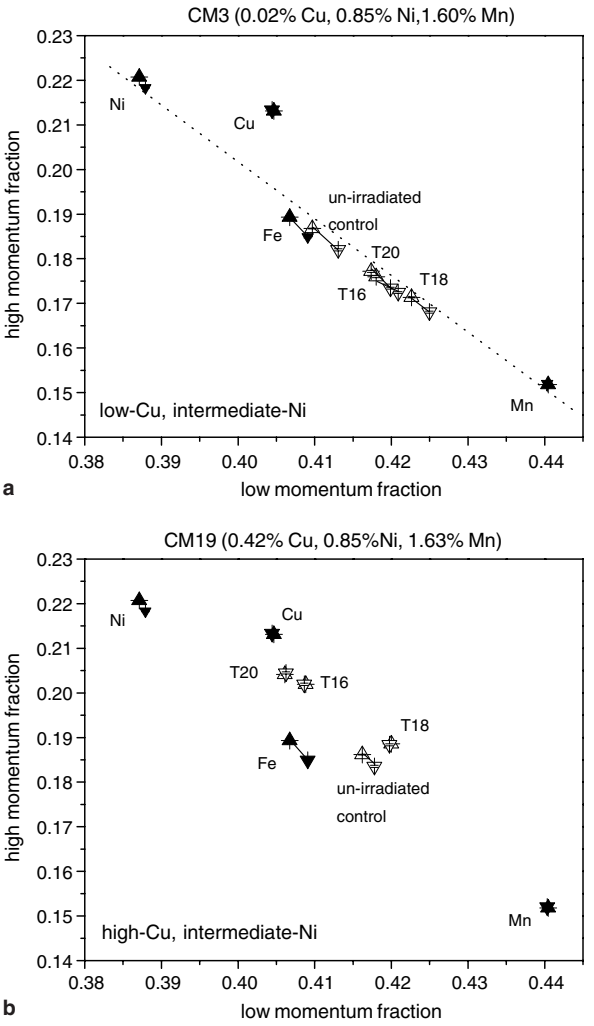

Fig. 3. Results of the spin-polarized, magnetic positron annihilation measurements for the (a) low-Cu, intermediate-Ni (CM3) and (b) high-Cu, intermediate-Ni (CM19) steels. Positron annihilation fraction in the high-momentum region (1 a.u. $\leqslant p_L \leqslant$ 4 a.u.) versus the low-momentum region ($p_L \leqslant 0.382$ a.u), normalized to the total annihilations, for the magnetic field oriented parallel (up-triangle) and anti-parallel (down-triangle) to the positron polarization. Elemental Fe, Cu, Ni, and Mn are shown with solid symbols. The line in (a) is drawn to guide the eye.

and bigger low-momentum fraction. The *S*–*W* data points move further in the direction of Mn (and/or Si and vacancies) with decreasing irradiation temperature.

There is no unique interpretation that can be applied to these results. However, they are broadly consistent with *some* positron annihilation at very small vacancy-Mn–Si–Ni–Fe complexes. The balance of annihilations occurs in the Fe-matrix. The strongest evidence of the involvement or

irradiation-induced features in the shifts in the direction of Mn, Si and vacancies, and that the vacancy and/or Mn-Si content would be expected to increase with decreasing temperature. However, lifetime measurements are needed to determine the relative involvement of vacancies versus Mn, Fe and Ni. Nevertheless, assuming there is trapping taking place, vacancies and/or vacancy-solute clusters are likely to be present. It may also be possible that small features composed of Ni–Si–Mn–Fe clusters could both trap positrons and yield the observed *S*–*W* data point trends. The splitting can be explained by the presence of both Ni and Fe in the dilute clusters and their very small size, resulting in incomplete positron localization in the feature itself, as well as competing annihilations in the Fe matrix.

The splitting observed in the *S*–*W* plot in unirradiated high-Cu, intermediate-Ni steel (CM19) shown in Fig. 3(b), is smaller than that in the unirradiated low-Cu, intermediate-Ni steel (CM3) in Fig. 3(a). This may be due to positron trapping in some Cu–Ni–Mn clusters formed during the heat treatment prior to irradiation. Similar behavior is observed in other Cu-bearing steels (CM16, CM17 and CM20). Following irradiation of the high-Cu, intermediate-Ni steel (CM19) at temperatures from 270 to 310 °C to 1.6×10^{23} n m^{-2}, the spin-polarized data points fully overlap and do not show any splitting. This indicates that essentially all the annihilations occur at trapping sites with non-magnetic atoms. The position of the points on the *S*–*W* plot depends on the irradiation temperature. At 290 and 310 °C, the points indicate features highly

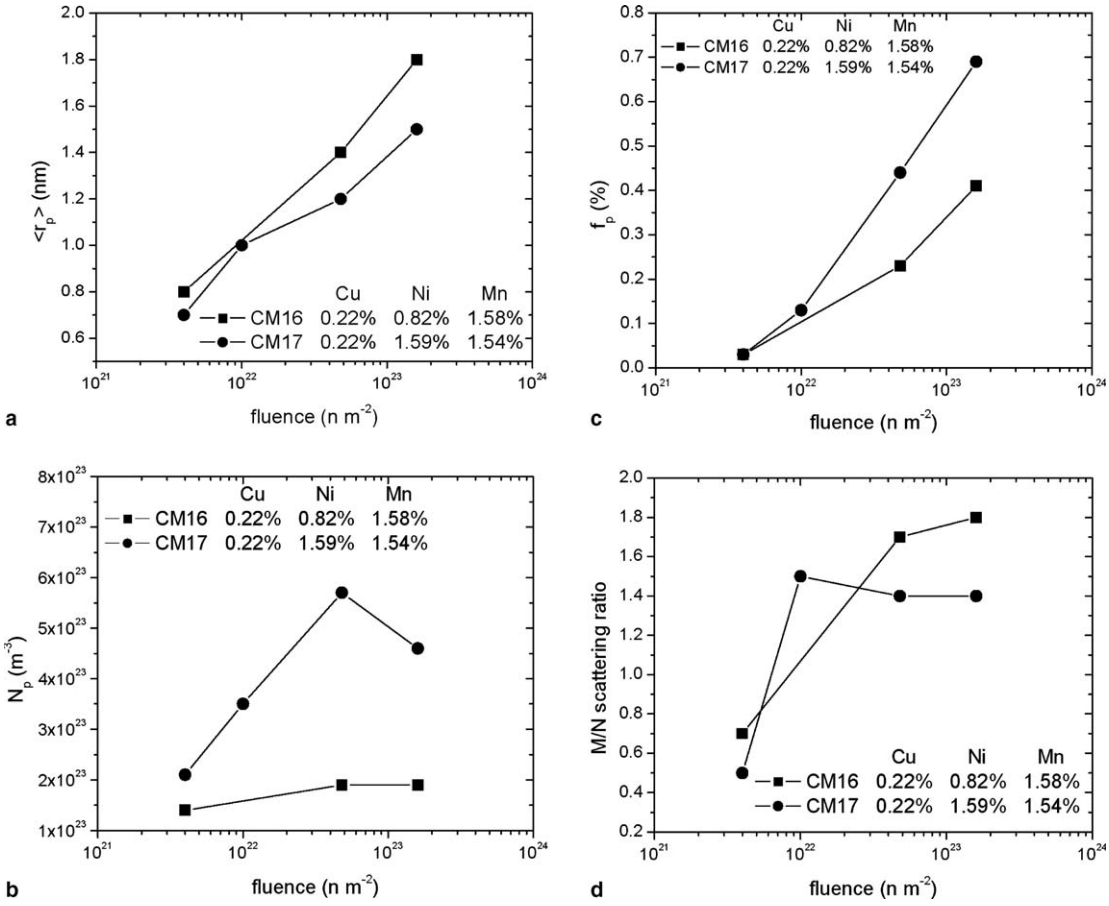

Fig. 4. Results of SANS data analysis for the intermediate-Cu, intermediate-Ni (CM16) and the intermediate-Cu, high-Ni (CM17) steels with increasing fluence: (a) mean radius ($\langle r \rangle$), (b) number density (N_p), (c) volume fraction of scattering features (f_p), and (d) magnetic to nuclear (M/N) scattering ratio. The intermediate-Cu, intermediate-Ni steel (CM16) at the 1.0×10^{22} n m^{-2} irradiation fluence (T12) was not measured. All irradiations were performed at 290 °C, with flux variations as indicated in the figure and in Table 1. The lines are drawn to guide the eye.

enriched in Cu and Ni with a third element known to be Mn. The *S–W* points for the 270 °C irradiation fall on or near a line connecting Cu and a larger amount of Mn (or alternately Si or vacancies or vacancy clusters), although this does not preclude the presence of Ni as well. The *S–W* plots for the other Cu-bearing CM-series steels (CM16, CM17 and CM20) are very similar to the results shown in Fig. 3(b).

3.2. SANS results

Fig. 4 summarizes the SANS data for the intermediate-Cu steels with intermediate (CM16 with 0.22% Cu, 0.82% Ni) and high Ni (CM17 with 0.22% Cu and 1.59% Ni) contents irradiated at 290 °C over a range of fluences. Fig. 4(a) shows that the mean precipitate radii, $\langle r \rangle$, increases with increasing fluence, and are smaller for the high Ni (CM17) alloy. Fig. 4(b) shows the precipitate number density, N_p, is systematically higher in the high Ni (CM17) steel, with a peak at intermediate fluence. The N_p in the intermediate Ni (CM16) steel increases slowly and monotonically with increasing fluence. Note in all cases, the N_p are high with values in excess of 10^{23} m^{-3}. As shown in Fig. 4(c), the precipitate volume fraction, f_p, increases continuously with fluence. The f_p is significantly larger in the high-Ni (CM17) versus intermediate-Ni (CM16) steel at higher fluence, but are similar at low fluence. Fig. 4(d) shows that the magnetic to nuclear scattering ratios, M/N, initially increase, but are approximately constant at fluences above $\approx 10^{22}$ n m^{-2}. Note the SANS data are less reliable at the lowest fluence for the features due to their small size $\langle r_p \rangle$ and f_p. The M/N are generally lower in the high-Ni steel (CM17), indicating that increasing the alloy Ni content increases the concentration of both Ni and Mn in the precipitates, consistent with other measurements [1,2,32,33].

Fig. 5 shows the corresponding plots of the SANS data for all the Cu-bearing steels as a function of irradiation temperature from 270 to 310 °C. The results can be summarized as follows:

- The precipitate $\langle r_p \rangle$ increase and N_p decrease with increasing temperature (Fig. 5(a) and (b)).
- The coarsening of the precipitate structure with increasing temperature is generally accompanied by modest reductions in f_p (Fig. 5(c)).
- The precipitate $\langle r_p \rangle$ decreases, while the N_p and f_p increase with increasing Ni (Fig. 5(a)–(c)).
- The f_p exceed the atomic fraction of the initially dissolved Cu content of the alloys, estimated to be ≈0.19% and 0.22–0.29% for the intermediate and high-Cu steels, respectively (Fig. 5(c)).
- The M/N increases with increasing irradiation temperature and decreasing alloy Ni content, consistent with increasing precipitate Cu content (Fig. 5(d)).

These results are generally consistent with previous observations [32,33].

4. Discussion and summary

Both the PAS and SANS measurements show the formation and growth of Cu–Ni–Mn precipitates in Cu-bearing steels. First consider the high fluence data at 290 °C. Increasing the alloy Ni content from about 0.8% to 1.6% increases f_p and refines the precipitate distribution with an increased N_p. The increase in f_p is associated with higher Mn and Ni content of the precipitates as reflected in lower M/N ratios of 1.45 ± 0.05. This nominal M/N results from a precipitate composed of approximately equal quantities of Cu, Ni and Mn. Assuming that the Cu is nearly fully precipitated, this composition estimate is also compatible with the measured volume fractions in the high-Ni alloys (CM17 and CM20); the high-Ni steels with intermediate and high-Cu initially contain ≈0.19% and 0.28% atom fraction of dissolved Cu, respectively, which are ≈28% and 33% of the corresponding total f_p of ≈0.68% and 0.86%. A similar analysis of the intermediate-Ni steels (CM16 and CM19) yields consistent precipitate compositions of ≈44% Cu and 28% of each Ni and Mn. Notably, in all these cases, the irradiation-induced features are MNPs rather than CRPs. Finally, the precipitate Mn and Ni contents increase with decreasing irradiation temperature and vice versa. We have not considered Si, which would produce scattering contrast similar to a mixture of 2/3Mn and 1/3Ni. However, these alloys have low Si content and the amount of Si present in the precipitates is expected to be modest.

At first glance, the lower sensitivity of the OEMS to composition and temperature variations may seem puzzling. However, this behavior can be readily rationalized by noting the competing effects of Mn (and Si) versus Ni on the magnitude of the OEMS peak along with preferential annihilations in Cu and to a lesser extent Ni versus Mn due to different elemental affinities, as well as precipitate

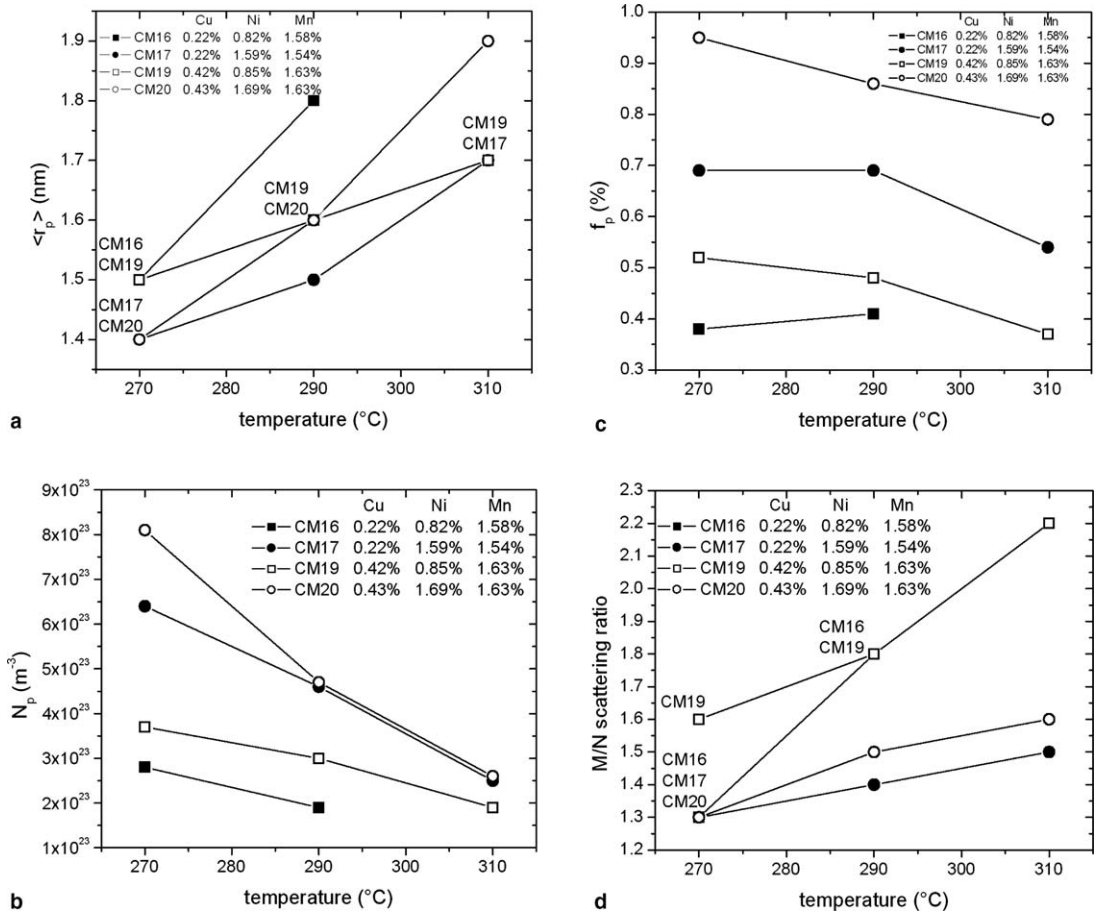

Fig. 5. Results of SANS data analysis for the intermediate/high-Cu and intermediate/high-Ni steels (CM16, CM17, CM19, and CM20) with varying temperature: (a) mean radius ($\langle r \rangle$), (b) number density (N_p), (c) volume fraction of scattering features (f_p), and (d) magnetic to nuclear (M/N) scattering ratio. Some data points in Fig. 5(a) and (d) superimpose each other. The intermediate-Cu, intermediate-Ni steel (CM16) at the 310 °C irradiation condition (T20) was not measured. The average fluence of the irradiations is 1.6×10^{23} n m^{-2}. See Table 1 for specific irradiation conditions. The lines are drawn to guide the eye.

structures consisting of almost fully Cu-rich cores surrounded by Ni, Mn and Si enriched shells. The broad consistency of the OEMS and SANS results is encouraging. However, a more important observation is the complete lack of magnetic splitting in the precipitate trapping features observed in the spin-polarized positron measurements. This observation indicates the absence of significant quantities of Fe and Ni in the annihilation region. However, this does not mean that the features do not contain Ni along with Mn and even some small amount of Fe in the shell region.

There is an open question about Mn and Si versus vacancy source of the enhancement of the low-momentum region in the 270 °C irradiations that can only be resolved by lifetime measurements that will be carried out in the future. While other details of the data on Cu-bearing steels could be discussed, in summary, all of the SANS and PAS observations are highly consistent with previous results based on a variety of characterization techniques in addition to existing theoretical understanding and models of the evolution of precipitate structures in irradiated RPV steels [1–4,6,12,13,19,24–26]. The one key exception to this overall consistency, is the apparent presence of Fe within the precipitate cores, as found in atom probe tomography studies.

The OEMS of the low-Cu, intermediate-Ni steel (CM3) exhibit a weak signal probably associated with some annihilations at small vacancy-Mn–Ni–Si-Fe complexes. The presence of vacancies, Si and Mn are qualitatively consistent with the OEMS signature, while vacancies, Si and Ni would make the feature an attractive trapping site. The corre-

sponding SANS data was generally too weak and scattered to fit reliably. The strongest scattering was observed in the 270 °C irradiation to the highest fluence, which indicates the presence of very small volume fraction with $f \approx 0.028\%$ (nominal value assuming that the feature is non-magnetic) of extremely small features, with $\langle r \rangle \approx 0.5$ nm and characterized by a low M/N ratio of ≈1. Combined resistivity and Seebeck coefficients are consistent with a volume fraction, $f \approx 0.17\%$ of Ni–Mn–Si clusters [19], not including any associated vacancies. The SANS and OEMS data are roughly consistent with a very high density $\approx 4 \times 10^{24}$ m^{-3} of small ≈0.5 nm features, that remain partially magnetic (≈50% of the ferrite matrix), composed of ≈50% Fe with the balance split between Ni, Mn and Si (probably a higher fraction of Ni) plus one to a few vacancies. Such features would be expected to: (1) manifest only weak magnetic and nuclear small angle neutron scattering; (2) trap positrons and yield a weighted OEMS with a small minimum at higher momentum and enhancement at low momentum that manifest magnetic splitting; and (3) roughly account for the amount of solute removal from the matrix as estimated from the RSC measurements. Notably, there is no evidence of the development of well-formed, highly enriched MNPs in the low-Cu, intermediate-Ni steels (CM3).

Positron lifetime measurements will be needed to further assess the validity of the hypothesis about the character of matrix features outlined above. However, it is noted that these conclusions are generally consistent with the combined OEMS and lifetime observations of small vacancy cluster complexes in simple Fe–1%Mn alloys irradiated at 290 °C [12,31].

Acknowledgements

This work was partially supported by the US Nuclear Regulatory Commission under contracts #04-94-049 and 04-01-064, and partially performed under the auspices of the US Department of Energy by the University of California, Lawrence Livermore National Laboratory under Contract No. W-7405-Eng-48. We acknowledge the support of the National Institute of Standards and Technology, Center for Neutron Research, in providing the neutron research facilities used in this work, and the major contributions of D. Klingensmith (UCSB).

References

[1] G.R. OdetteMaterials Research Society Symposium Proceedings, vol. 373, Materials Research Society, Warrendale, Pennsylvania, 1995, p. 137.
[2] G.R. Odette, G.E. Lucas, Radiat. Eff. Def. Solids 144 (1998) 189.
[3] G.R. Odette, G.E. Lucas, JOM 53 (2001) 18.
[4] G.R. Odette, Neutron Irradiation Effects in Reactor Pressure Vessel Steels and Weldments, International Atomic Energy Agency, Vienna, IAEA IWG-LMNPP-98/3, 1998, p. 438.
[5] G.R. Odette, B.D. Wirth, D.J. Bacon, N.M. Ghoneim, MRS Bull. 26 (2001) 176.
[6] G.R. Odette, T. Yamamoto, D. Klingensmith, Philos. Mag. 85 (2005) 779.
[7] G.S. Was, M. Hash, G.R. Odette, Philos. Mag. 85 (2005) 703.
[8] G.R. Odette, B.D. Wirth, J. Nucl. Mater. 251 (1997) 157.
[9] G.R. Odette, Scripta Metall. 11 (1983) 1183.
[10] A. Ulbricht, J. Boehment, P. Strunz, C. Dewhurst, M.H. Mathon, Appl. Phys. A – Mater. Sci. Process. 74 (2002) S1128.
[11] M. Grosse, J. Boehment, R. Gilles, J. Nucl. Mater. 254 (1998) 143.
[12] B.D. Wirth, G.R. Odette, P. Asoka-Kumar, R.H. Howell, P.A. Sterne, in: G.S. Was (Ed.), Proceedings of the 10th International Symposium on Environmental Degradation of Materials in Light Water Reactors, National Association of Corrosion Engineers, 2002.
[13] M.K. Miller, B.D. Wirth, G.R. Odette, Mater. Sci. Eng. A 353 (2003) 133.
[14] P. Pareige, K.F. Russel, R.E. Stoller, M.K. Miller, J. Nucl. Mater. 250 (1997) 176.
[15] M.K. Miller, P. Pareige, M.G. Burke, Mater. Charact. 44 (1–2) (2000) 235.
[16] B. Radiguet, P. Pareige, A. Barbu, Sur. Int. Anal. 35 (2004) 515.
[17] M.K. Miller, M.G. Burke, J. Nucl. Mater. 195 (1992) 68.
[18] P. Auger, P. Pareige, S. Welzel, J.C. Van Duysen, J. Nucl. Mater. 280 (2000) 331.
[19] G.R. Odette, C. Cowan, in: G.S. Was (Ed.), Proceedings of the 10th International Symposium on Environmental Degradation of Materials in Light Water Reactors, National Association of Corrosion Engineers, 2002.
[20] S. Ishino, Y. Chimi, Bagiyono, T. Tobita, N. Ishikawa, M. Suzuki, A. Iwase, J. Nucl. Mater. 323 (2003) 354.
[21] B. Acosta, F. Sevini, L. Debarberis, Int. J. Press. Vess. Piping 82 (2005) 69.
[22] Y. Nagai, M. Hasegawa, Z. Tang, A. Hempel, K. Yubuta, T. Shimamura, Y. Kawazoe, A. Kawai, F. Kano, Phys. Rev. B 61 (10) (2000) 6574.
[23] Y. Nagai, Z. Tang, M. Hassegawa, T. Kanai, M. Saneyasu, Phys. Rev. B 63 (2001) 134110.
[24] P. Asoka-Kumar, B.D. Wirth, P.A. Sterne, G.D. Odette, Philos. Mag. Lett. 82 (2002) 609.
[25] S.C. Glade, B.D. Wirth, G.R. Odette, P. Asoka-Kumar, P.A. Sterne, R.H. Howell, Philos. Mag. 85 (2005) 629.
[26] M. Hasegawa, Z. Tang, Y. Nagai, T. Chiba, E. Kuramoto, M. Takenaka, Philos. Mag. 85 (4–7) (2005) 467.
[27] P. Hautojärvi, C. Corbel, in: A. Dupasquier, A.P. Mills Jr. (Eds.), Positron Spectroscopy of Solids, Proceedings of the

International School of Physics, Course CXXV, Italian Physical Society, Bologna, Italy, p. 491.
[28] P. Asoka-Kumar, M. Alatalo, V.J. Ghosh, A.C. Kruseman, B. Nielsen, K.G. Lynn, Phys. Rev. Lett. 77 (1996) 2097.
[29] M.J. Puska, R.M. Nieminen, Rev. Mod. Phys. 66 (1994) 841.
[30] C.J. Glinka, J.M. Rowe, J.G. laRock, J. Appl. Crystallogr. 19 (1986) 427.
[31] B.D. Wirth, P. Asoka-Kumar, R.H. Howell, G.R. Odette, P.A. SterneMaterials Research Society Symposium Proceedings, vol. 650, Materials Research Society, Warrendale, Pennsylvania, 2001, p. R6.5.1.
[32] B.D. Wirth, On the Character of Nano-Scale Features in Reactor Pressure Vessel Steels Under Neutron Irradiation, Ph.D. Dissertation, University of California, Santa Barbara, 1998.
[33] E.V. Mader, Kinetics of Irradiation Embrittlement and the Post-Irradiation Annealing of Nuclear Reactor Pressure Vessel Steels, Ph.D. Dissertation, University of California, Santa Barbara, 1995.
[34] C.L. Liu, G.R. Odette, B.D. Wirth, G.E. Lucas, Mater. Sci. Eng. A 238 (1997) 202.
[35] S.C. Glade, B.D. Wirth, P. Asoka-Kumar, P.A. Sterne, G.R. Odette, Mater. Sci. Forum 445&446 (2004) 87.
[36] K. Dohi, N. Soneda, personal communication.